

Sound Velocities in Olivine at Earth Mantle Pressures

J. M. Zaug, E. H. Abramson, J. M. Brown,* L. J. Slutsky

The independent elastic constants of an upper mantle mineral, San Carlos olivine [(Mg_{1.8}Fe_{0.2})SiO₄], were measured from 0 to 12.5 gigapascals. Evidence is offered in support of the proposition that the explicit temperature dependence of the bulk modulus is small over the range of temperatures and pressures thought to prevail above the 400-kilometer discontinuity, and thus the data can be extrapolated to estimate the properties of olivine under mantle conditions at a depth of 400 kilometers. In the absence of high-temperature data at high pressures, estimates are made of the properties of olivine under mantle conditions to a depth of 400 kilometers. In contrast with low-pressure laboratory data, the predicted covariance of shear and compressional velocities as a function of temperature nearly matches the seismically estimated value for the lower mantle.

The interpretation of seismological measurements in terms of composition, temperature, and density requires knowledge of the elastic properties of the presumed constituents of the mantle at high pressure. However, data at pressures in excess of 3 GPa have not in general been available. Mineralogical models of the deep mantle (the pressure at the 400-km seismic discontinuity is approximately 13.5 GPa) have been constructed on the basis of extrapolation and analogy (1). Here we report measurements of the elastic properties of an important upper mantle constituent at appropriate pressures. Extrapolations based on pressure derivatives measured below 3 GPa do not represent the pressure dependence of either the longitudinal or the shear wave velocities accurately enough to permit the derivation of reliable compositional constraints from a comparison of extrapolated properties with observed seismic velocity profiles.

We loaded crystals of olivine cryogenically into a diamond-anvil cell (2), with argon as the pressure medium. The elastic constants (3) at 298 K (Fig. 1) were calculated from velocities measured by impulsive stimulated scattering (2, 4, 5), typically at 10° intervals in the *ab*, *ac*, and *bc* planes. The density at ambient pressure was determined from lattice constants and an x-ray microprobe analysis. Densities and lattice constants at high pressure were determined recursively; the measured velocities and approximate densities define approximate elastic compliances that permit calculation of more accurate high-pressure densities. The correction from adiabatic to isothermal moduli is small and easily estimated (5). The equation of state of olivine derived here is in agreement with that of a single crystal x-ray study (6).

Orientationally averaged (7) compressional and shear velocities from the constants in Fig. 1 are plotted in Fig. 2 (8). The parameters of polynomial representations of the pressure dependence of the bulk and shear moduli are given in Table 1. Our data agree with results for other olivine samples (9–11) in the common pressure range. However, at pressures above 10 GPa, disagreement between our data and the extrapolation of the lower pressure elas-

tic constants in some cases approaches 25%. At 13 GPa, differences between our measured velocities at room temperature and the extrapolated velocities of Duffy and Anderson (1) are comparable in magnitude to the size of the seismic discontinuity at 400 km (1) (Fig. 2) and to the differences among the velocities of appropriate mantle-candidate minerals.

To interpret the seismic velocity profile in the upper mantle, knowledge of velocities in candidate minerals is required at simultaneously high temperature and high pressure. Such data are not yet available. However, Chopelas (12) has investigated the pressure dependence of the Raman and infrared spectra of olivine, determined the volume dependences of the frequencies of vibrational modes of olivine, and constructed an approximate vibrational frequency distribution function. These results permit the calculation of the thermal pressure in the quasi-harmonic equation of state (13)

$$P + \frac{du}{dV} = \sum_i^N \frac{\gamma_i E_i}{V} \quad (1)$$

(where *P* is pressure; *V* is volume; γ_i and E_i are, respectively, the Grüneisen parameter and the vibrational energy of the *i*th mode; and *u* is the static lattice energy) and thus estimation of the density as a function of temperature and pressure from the room-temperature isotherm.

The similarity (Fig. 3) between the slope of the bulk modulus versus density measured in isothermal compression and that observed in (11) when olivine is heated at ambient pressure supports the notion that the bulk modulus is a function primarily of density and not explicitly of temperature. An explicit temperature derivative of the shear modulus is required. If the temperature dependence of the shear modulus at constant density is evaluated from the difference between the extrapolated isotherm and the measured isobar in Fig. 3, then the calculated compressional and shear velocities in olivine along a 1400°C adiabat (Fig. 2) suggest that the properties of olivine closely

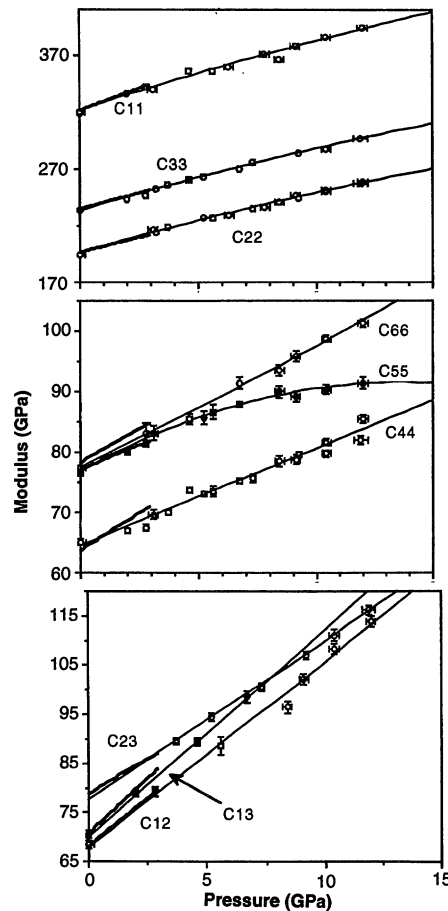


Fig. 1. The elastic constants of [(Mg_{1.8}Fe_{0.2})SiO₄] at 298 K as a function of pressure between 1 and 12.5 GPa (3). The light curves represent a quadratic fit to the pressure dependence of *c_p*, the heavy curves are the experimental results of Webb (9). The elastic constants reproduce the velocity data with a root-mean-square misfit of about 0.2%. Formal uncertainties for individual constants differ between experiments but are typically near 0.5%. The average misfit between data and the polynomial fits is 0.7%. Additional scatter may have been introduced through small errors in pressure measurement and crystallographic orientation or nonhydrostatic stresses.

Department of Chemistry and the Geophysics Program, University of Washington, Seattle, WA 98195.

*To whom correspondence should be addressed.

match the seismological upper mantle velocity structure. A similar conclusion was reached by Duffy and Anderson (1) on the basis of an overestimated pressure dependence of the moduli and a larger temperature derivative than that calculated here.

The value of $d\ln V_s/d\ln V_p$ derived here for olivine is compared with lateral variations of seismic velocities in the lower mantle in Table 2. Isaak (11) and others have argued on the basis of low-pressure data that this derivative is, for any given mineral, approximately independent of temperature. The disagreement between earlier laboratory values and the seismically determined covariance of velocities has been interpreted as evidence for lateral compositional heterogeneity in the mantle. The same conclusion could be justified on the basis of our room-temperature, high-pressure data alone. If the shear modulus at fixed density were taken to be independent of the temperature, $d\ln V_s/d\ln V_p = 1.1$. However, if the explicit temperature derivative of the shear modulus (required by simultaneous consideration of the high-temperature and high-pressure data) is included, the disparity between an

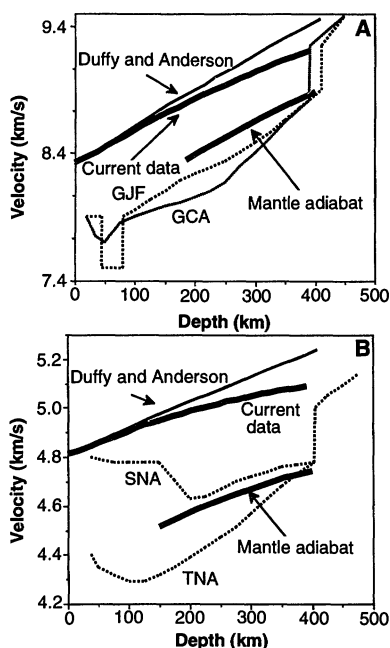


Fig. 2. Compressional (A) and shear (B) velocities as a function of depth. Hashin-Shtrikman bounded compressional and shear wave velocities at 298 K are derived from the measured elastic constants. The width of the curves span the upper and lower bounds of the measured error. At 13 GPa, the extrapolated bulk modulus is 4% greater than the experimental value; the measured and extrapolated shear moduli differ by 6%. Properties of olivine under mantle conditions of pressure and temperature are shown along a 1400°C adiabat. For comparison, high-resolution seismic profiles [TNA and SNA are from (15), GCA is from (16), and GJF is from (17)] are also shown.

Table 1. Polynomial fit to the average of the Hashin-Shtrikman bounds for the adiabatic elastic constants of San Carlos olivine as a function of pressure along the 298 K isotherm; M , modulus. The ambient pressure crystal density is 3.362 Mg m^{-3} . No uncertainty estimates are given for the coefficients. Instead a nominal 0.5% uncertainty is assigned to calculated moduli. The coefficients should provide an accurate interpolation rule for olivine elasticity to 13 GPa.

Modulus	Initial value (GPa)	dM/dP	d^2M/dP^2 (GPa^{-1})
Bulk modulus	129.0	4.56	-0.051
Shear modulus	77.6	1.71	-0.061

estimate based on Fig. 3 and the seismic result is small. The seismic velocity covariance can then be consistently interpreted in terms of lateral variations in temperature associated with mantle convection.

The derivatives (Table 2) $d\ln V_p/d\ln \rho$ and $d\ln V_s/d\ln \rho$ reflect at constant pressure the dependence of velocity on density and thus temperature. In the context of mantle dynamics they provide a measure of the horizontal variation of density in the mantle (caused by temperature differences) based on observed differences in velocity. Seismic tomography provides high-resolution images of velocity but not density. It is, however, density perturbations that are the driving force for mantle convection (14). At high pressure and temperature, shear velocities in olivine are more sensitive to density variation than compressional velocities. The data (Table 2) suggest that a 1% increase in density corresponds to a 2% increase in the

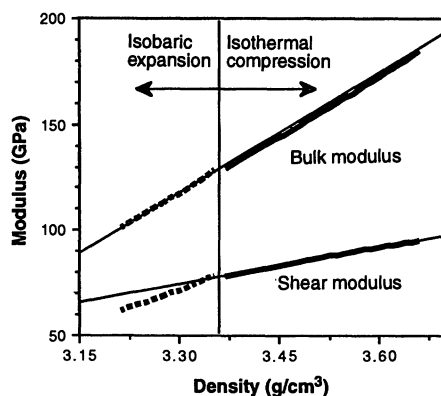


Fig. 3. The Hashin-Shtrikman bounded bulk and shear moduli as functions of density. The high-density portion of the curves are from our data (compression at 298 K), and the low-density portions are from Isaak (11) (heating at 1 bar). Linear fits to the data demonstrate that the bulk modulus is linear in density. The difference in slopes for the shear modulus between expansion and compression is interpreted as a constant-volume temperature derivative of the modulus.

Table 2. Derivatives at constant pressure of compressional and shear velocities (V_p and V_s) for olivine and the lower mantle. The implicit independent variable is temperature.

Derivative	Value		
	1 bar, 1100°C*	13 GPa, 1400°C†	Lower mantle‡
$d\ln V_p/d\ln \rho$	1.7	1.1	
$d\ln V_s/d\ln \rho$	2.2	2.1	
$d\ln V_s/d\ln V_p$	1.3	1.8	$2.3_{-0.6}^{+0.3}$
$\frac{dV_p}{dT} \times 10^4$ $\text{km s}^{-1} \text{K}^{-1}$	-5.3	-2.9	
$\frac{dV_s}{dT} \times 10^4$ $\text{km s}^{-1} \text{K}^{-1}$	-3.7	-2.8	

*Calculated from the highest temperature data in (11). †Calculated using current high-pressure data. ‡From (18).

shear wave velocity. Typical variations are about 1% total in shear wave velocities. Changes in compressional and shear wave velocities of 1% require, respectively, temperature changes of 300°C and 170°C.

The problems of extrapolating low-pressure data demonstrated here for olivine argue against extrapolation to mantle conditions of low-pressure velocities in other candidate constituents (principally pyroxene and garnet phases) to construct a compositional or dynamical model for the upper mantle. Even with high-pressure data at room temperature, the uncertainties in the temperature derivatives are large enough that velocity at mantle conditions cannot be determined accurately. Without appropriate data for other high-pressure silicates, it is premature to infer compositional variability across the 400-km discontinuity on the basis of mineral elasticity. Measurement of the temperature dependence of the elastic properties of mantle candidate minerals at high pressure (particularly studies of the temperature dependence of shear velocities at constant density) would appear to be essential before velocities can reliably be interpreted in terms of chemical composition or driving forces for mantle convection. With the aid of the experimental techniques reported here, this problem can be addressed in heated diamond anvil cells.

REFERENCES AND NOTES

1. The presumed cause of the seismic discontinuity at a depth of 400 km is the equilibrium phase transition between olivine and the high-pressure β -phase silicate spinel. However, other changes in composition may also be required [T. S. Duffy

- and D. L. Anderson, *J. Geophys. Res.* **94**, 1895 (1989); D. L. Anderson, *ibid.* **93**, 4688 (1988); C. Bina and B. J. Wood, *ibid.* **92**, 4853 (1987); D. J. Weidner, in *Chemistry and Physics of Terrestrial Planets*, S. K. Saxena, Ed. (Springer-Verlag, New York, 1986), pp. 251–274; S. M. Rigden, G. D. Gwanmesia, J. D. FitzGerald, I. Jackson, R. C. Liebermann, *Nature* **354**, 143 (1991)].
- J. M. Brown, L. J. Slutsky, K. A. Nelson, L.-T. Cheng, *J. Geophys. Res.* **94**, 9485 (1989).
 - Elastic constants are elements of a second-order tensor relating the six independent components of stress to those of infinitesimal strain. Various relationships reduce the number of required elastic constants to nine for a mineral of orthorhombic symmetry.
 - M. D. Fayer, *IEEE J. Quantum Electron.* **22**, 1444 (1986); Y. X. Yan, L.-T. Cheng, K. A. Nelson, in *Advances in Non-Linear Spectroscopy*, J. H. Clark and R. E. Hester, Eds. (Wiley, London, 1987), pp. 1437–1452; K. A. Nelson, R. Casalegno, R. J. Dwayne Miller, M. D. Fayer, *J. Chem. Phys.* **77**, 1144 (1982); J. M. Brown, L. J. Slutsky, K. A. Nelson, L.-T. Cheng, *Science* **241**, 65 (1988).
 - J. M. Zaug, E. H. Abramson, J. M. Brown, L. J. Slutsky, in *High Pressure Research: Applications to Earth and Planetary Sciences*, Y. Syono and M. H. Manghnani, Eds. (American Geophysical Union, Washington, DC, 1992), pp. 157–166.
 - Y. Kudoh and Y. Takeuchi, *Z. Kristallogr.* **171**, 291 (1985).
 - We use the Hashin-Shtrikman bounds [P. J. Watt, *J. Appl. Phys.* **50**, 6290 (1979)].
 - The conversion from pressure to depth is based on seismic model PREM [A. M. Dziewonski and D. L. Anderson, *Phys. Earth Planet. Inter.* **25**, 297 (1981)].
 - S. Webb, *Phys. Chem. Minerals* **16**, 684 (1989).
 - M. Kumazawa and O. L. Anderson, *J. Geophys. Res.* **74**, 5961 (1969).
 - D. G. Isaak, *ibid.* **97**, 1871 (1992).
 - A. Chopelas, *Phys. Chem. Minerals* **17**, 149 (1990).
 - M. Born and K. Huang, *Dynamical Theory of Crystal Lattices* (Clarendon, Oxford, 1954).
 - B. H. Hager, M. A. Richards, R. P. Cormier, A. M. Dziewonski, *Nature* **313**, 541 (1985).
 - S. P. Grand and D. V. Helmberger, *Geophys. J. R. Astron. Soc.* **76**, 399 (1984).
 - M. C. Walck, *ibid.*, p. 697.
 - _____, *ibid.* **81**, 243 (1985).
 - X.-D. Li, D. Giardini, J. H. Woodhouse, *Geophys. J. Int.* **105**, 649 (1991).
 - Partial support for this work was provided by the National Science Foundation (grant EAR-8804897). Additional support was provided by the University of Washington (Chemistry Department, Geophysics Program, College of Arts and Sciences). A Chevron Graduate Fellowship (J.M.Z.) is also acknowledged.

12 November 1992; accepted 19 April 1993

Direct Imaging of the Diacetylene Solid-State Monomer-Polymer Phase Transformation

Jun Liao and David C. Martin*

The solid-state phase transformation from 1,6-di(*N*-carbazolyl)-2-4-hexadiyne (DCHD) diacetylene monomer to polymer has been studied dynamically by low-dose selected area electron diffraction and high-resolution electron microscopy. The total exposure required to induce polymerization is five orders of magnitude smaller than the critical dose for electron beam damage. The phase transformation is quasi-homogeneous, with the lattice parameters changing continuously as a function of beam dose. Characteristic streaking that develops in the selected area electron diffraction patterns in the [200] reciprocal directions during the intermediate stages of the transformation provides information about the defect-mediated mechanisms of this reaction.

In the last two decades, the lattice-controlled solid-state polymerization of diacetylenes has attracted considerable attention. This route can be used to prepare crystals of poly(diacetylenes) of macroscopic size with the chains in an extended conformation (1). These single crystals of fully conjugated macromolecules have become model materials for investigating the physics of one-dimensional optical and electrical phenomena in organic polymers (2). The mechanisms of the phase transformation from diacetylene monomer to polymer have been examined by x-ray diffraction (3–6), x-ray topography (7, 8), and polarized optical microscopy (5). Thermal polymerization is usually found to be heterogeneous, whereas radiation polymerization by ultraviolet

light, γ -rays, or x-rays is often homogeneous. The intermediate transition states between monomer and polymer have also been studied by x-ray diffraction (3–5). However, because of the limited resolution of these techniques, the manner in which the phase transformation proceeds at the molecular level has remained unclear.

High-resolution information about materials structure is usually obtained by selected area electron diffraction (SAED) and high-resolution electron microscopy (HREM). Dynamic SAED and HREM are commonly used for studying inorganic systems (9). However, as is typical for organic materials, diacetylene monomers and polymers are sensitive to electron beam damage. Nevertheless, direct imaging by transmission electron microscopy (TEM) has been used in characterizing defects in certain polydiacetylene systems (10–12).

In the present study, we used the electron

beam in the TEM to induce the monomer-polymer phase transformation in DCHD. We imaged this solid-state process in situ as a function of dose in a JEOL 400-kV high-resolution electron microscope equipped with a Gatan yttrium-aluminum-garnet (YAG) crystal video recording system and image intensifier (13). Both the DCHD monomer and polymer crystals are monoclinic: the monomer has a space group of $P2_1/c$ with $a = 1.760$ nm, $b = 1.360$ nm, $c = 0.455$ nm, and $\gamma = 94.0^\circ$; the polymer has the same space group with $a = 1.739$ nm, $b = 1.289$ nm, $c = 0.490$ nm, and $\gamma = 108^\circ$ (14). We follow the convention for crystalline polymers in which the chain direction is parallel to the c axis.

The most critical factor in conducting this dynamic observation is the electron dose required to transform the monomer to polymer (J_{mp}). We determined J_{mp} by measuring the change in the electron diffraction pattern as a function of time at a given electron beam current on the sample and magnification (15). For DCHD, we found J_{mp} to be 1×10^{-4} C cm $^{-2}$ at 400 kV, which is five orders of magnitude smaller than the critical end-point dose J_c measured as 20 C cm $^{-2}$ at 200 kV for the 010 reflection (11, 16, 17). Extraordinary care must be taken to reduce the incident dose rate and avoid illuminating the sample with any more electrons than are absolutely necessary.

By selecting different condenser aperture sizes and electron beam spot sizes, we were able to control the electron dose rate on the samples at 1×10^{-5} C cm $^{-2}$ s $^{-1}$. Under these conditions, it takes 10 s for the DCHD monomer to be transformed into the polymer by the electron beam, which provides enough time to image the intermediate states of the transformation in detail with SAED. Recording an HREM image is possible with a spot size just sufficient to illuminate the YAG crystal (25 mm in diameter). This procedure minimizes the electron dose on the samples and makes it convenient to prefocus on an area adjacent to the area of interest in the minimum dose system. It also makes it possible to monitor the HREM images dynamically and record them on video tape. Our videos were digitized with a Scion video image 1000 board on a Mac II and analyzed by the "Image" processing program (18).

Molecular projections of the DCHD monomer and polymer in the [001] directions are shown in Fig. 1, A and F, respectively. A series of SAED patterns showing how the corresponding reciprocal lattices change during the monomer-polymer phase transformation are shown in Fig. 1, B to E. Figure 1B was taken at the beginning of the transformation and indexed as the [001] zone of the DCHD monomer. The pattern started to change at $J = 1 \times 10^{-5}$ C cm $^{-2}$, when γ increased and the lattice parameters a and b decreased. At J

Department of Materials Science and Engineering, College of Engineering, University of Michigan, Ann Arbor, MI 48109-2136.

*To whom correspondence should be addressed.